Supplementary Information

Magnetic propulsion of microswimmers with DNA-based flagellar bundles

Alexander M. Maier, Cornelius Weig, Peter Oswald, Erwin Frey, Peer Fischer & Tim Liedl

Supplementary Videos:

Supplementary Video 1. The video shows a close-up of the rotation of the swimmer demonstrated in Figure 2a. The video frame co-moves with the swimmer, so that the artificial tile-tube bundle swimmer stays in the center. The swimmer was actuated at 1Hz.

Supplementary Video 2. The video shows the directed motion of the swimmer from Figure 2b. The driving frequency was 1Hz and the rotation was along the horizontal axis. In addition to the forward swimming, a movement perpendicular to the rotation axis due to hydrodynamic drag with the close-by surface can be observed. The video is threefold accelerated.

Supplementary Video 3. The video shows the structural change of the artificial bundle upon changing the rotation frequency. By switching from 3Hz to 1Hz, the initially straight bundle changes to a chiral shape, which then propels the swimmer. The video is threefold accelerated.

Supplementary Video 4. The video shows the swimming along a curved path of the swimmer from Figure 2c. By gradually changing the rotation axis of the external magnetic field the swimming path can be controlled. The swimmer was driven at 1Hz. The video is eightfold accelerated.

Supplementary Video 5. The video shows a swimmer exposed to a rotating magnetic field along the horizontal axis that repeatedly switches from clock- to counterclockwise. The swimmer retains its forward motion while moving up and down due to a reversed interaction with the surface. The swimmer was driven at 1Hz. The video is threefold accelerated.

Supplementary Video 6. The video shows the analytic solution for the shape of a swimmer with decreasing tail stiffness. The colour code and the width of the tail indicate the local stiffness. In the front and rear view it becomes apparent that the tail has a static chiral structure.

Supplementary Note S1: Design and construction of DNA tile-tube - magnetic bead hybrids

Design of DNA tile tube structures. DNA tile tubes were constructed according to Yin et al.[1]. The shape and the stiffness of the DNA tile-tubes were controlled by adjusting the number of DNA strands, where *n* strands form a *n*-helix tube, and by changing their respective lengths. Depending on the design, the DNA strands had a length of 42 or 43 base pairs where each oligonucleotide was partially complementary to two adjacent strands. An even number n of strands leads to straight tubes with a stiffness that increases with the 4th power of the tube radius[2]. The st8HT from Figure 1d, for example, has a diameter of ~8 nm, a persistence length of ~8.2 μm, and readily polymerizes to a length of several micrometers. Elongating one of the n strands by inserting an additional base pair gives the assembled tubes a controlled pre-defined twist and curvature[3]. For example, the insertion of one base pair per structural unit in any double strand of an 8HT results in an overall helical shape (see Figure S1). The resulting helical structures (tw8HT) shown in Figure 1e exhibit a pitch and a diameter of sub-micrometer size. Larger diameter helices assemble when an odd number of DNA duplexes are used in the DNA tile tubes introducing a so-called "supertwist"[2]. Here the repeating structural unit assembles into a bundle with its neighboring units introducing a small relative twist to the DNA duplexes that causes the overall supertwist (as illustrated in Figure 1b). For example, the st13HT, shown in Figure 1f with a tube diameter of ~11 nm, shows a helical diameter of about 1 μm.

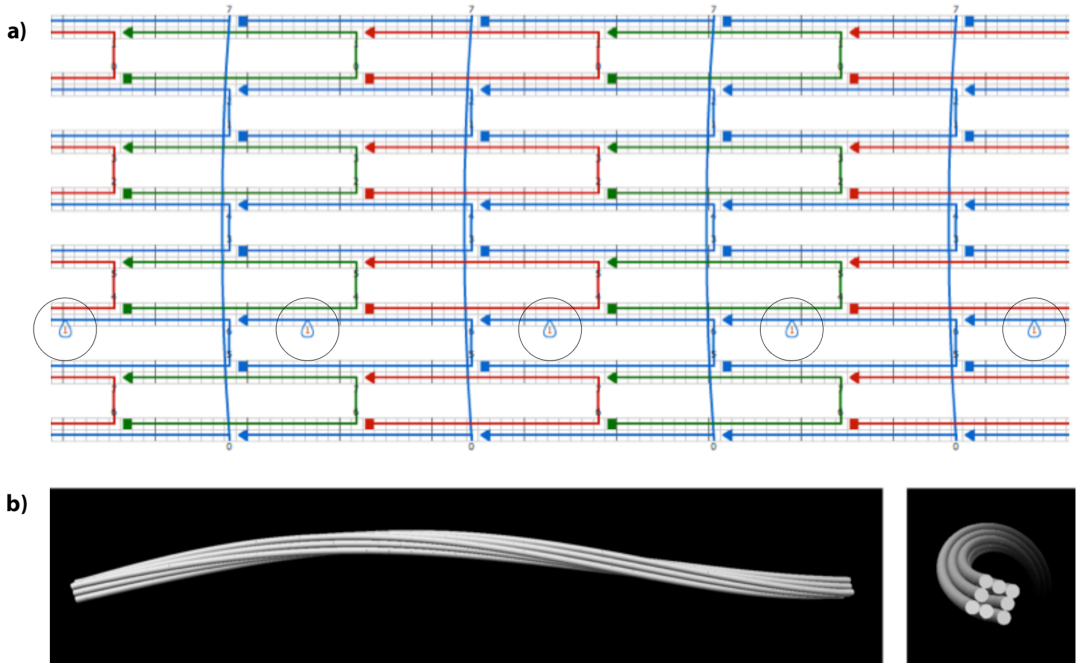

Figure S1: Design and simulation of twisted 8-helix tile tube. a) For a defined twist in the 8-helix tube (8HT), one extra base pair was added into every repeating segment of one double helix (illustrated by the blue loop). **b)** A cando[4] simulation shows the overall twist in the structure.

Folding and purification of DNA-tile tube structures. Assembly of the tile tube structures was carried out in a one-pot reaction with 1 μM of each oligonucleotide in 1x TAE buffer and 12 mM $MgCl_2$. The folding mixture was then exposed to a thermal annealing ramp, starting with a heating step to 80°C for 10 min, followed by a stepwise cooling from 65°C to 45°C at a cooling rate of 0.5°C / 5 min. (folded tile tube structures are shown in Figure S2-S4). After folding, larger tile tube structures were separated from smaller constructs via agarose gel electrophoresis (Fig. S3).

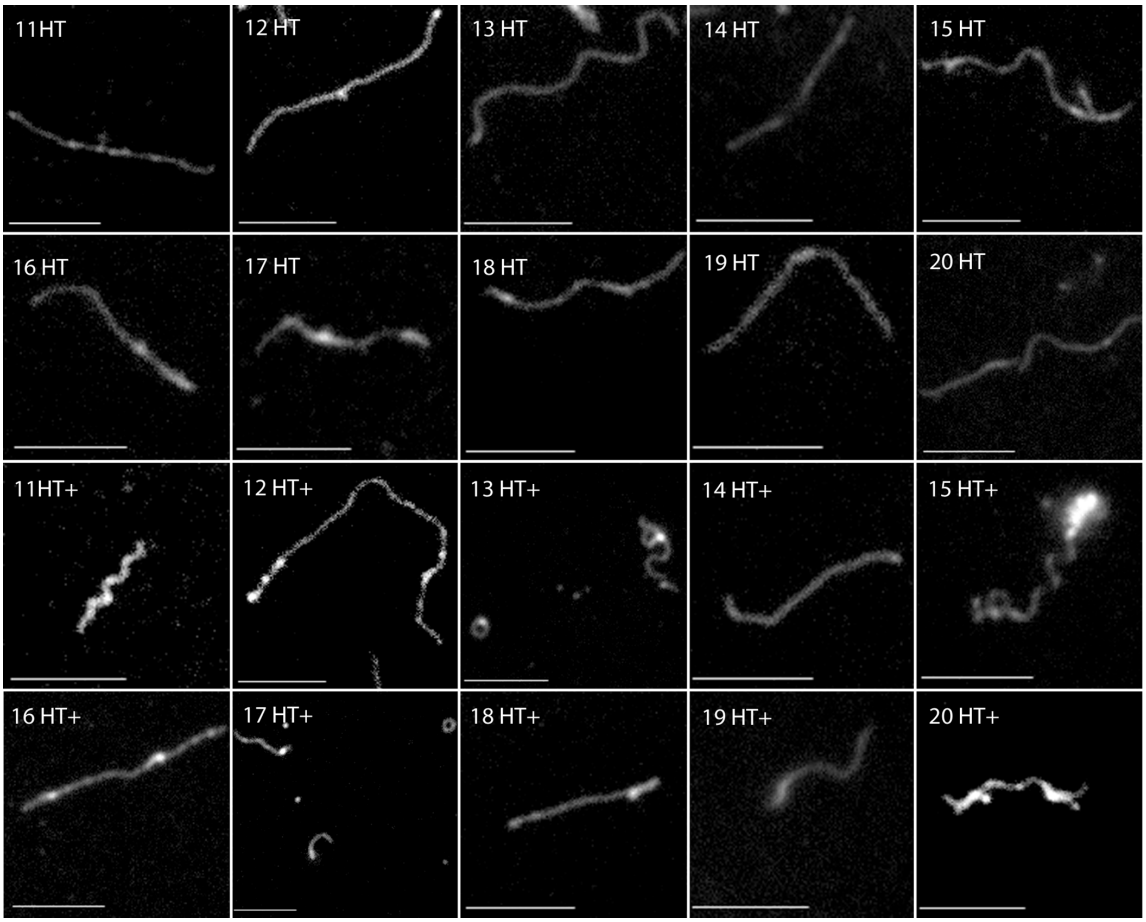

Figure S2: DNA tile tubes. Beside the structures presented in the main text (Fig. 1), DNA tile tubes were constructed that consisted of 11 to 20 double helices (11HT-20HT). In addition, we introduced an intrinsic twist (11HT+-20HT+) as is shown for the 8HT+ in Figure 1. This shows the great versatility in constructing helical shapes and bending stiffnesses easily accomplished by this method. All scale bars: 3 μm

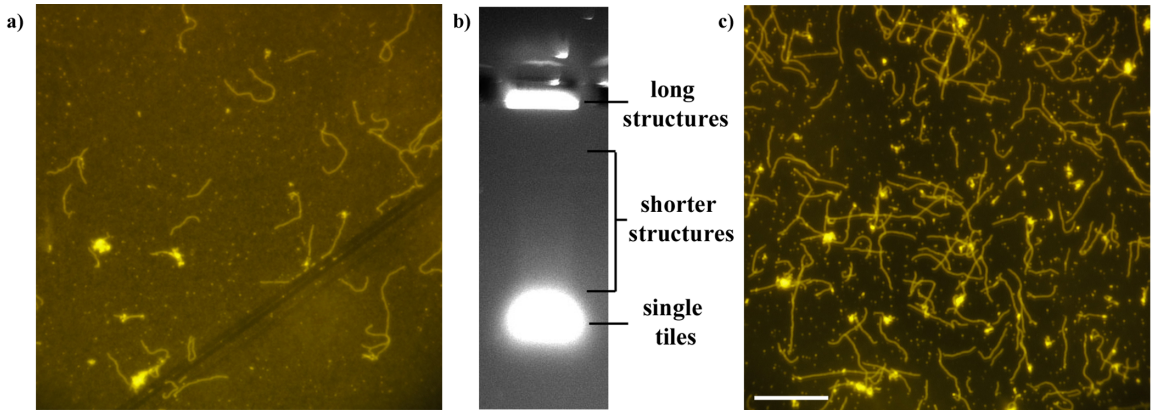

Figure S3: Purification of large tile tubes from smaller constructs. a) Fluorescence microscopy image of unpurified tile tubes taken directly after folding. The image shows a high background that can be attributed to light emitted by nanometer-sized tile tubes and unfolded oligonucleotides. **b)** In a 0.5% agarose gel, long tile-tube structures remain in the gel pocket and can be purified from smaller constructs and excess of single tiles. **c)** After purification of the sample, the background signal is drastically reduced. This separation of larger tile tubes is achieved by letting smaller constructs run into the gel, while larger structures remain in the pocket and can be pipetted out. Scale bars: 10 μm

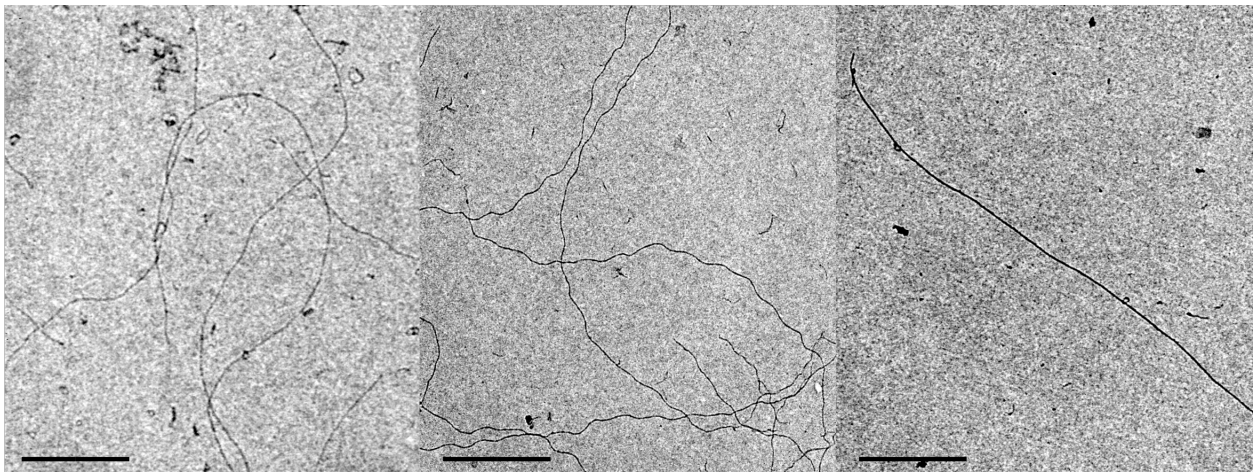

Figure S4: Structural characterization of purified tile-tubes. Correct folding of **a)** 8HT, **b)** tw8HT and **c)** 13HT as revealed by transmission electron microscopy. Scale bars: 1 μm

Magnetic particle - DNA conjugation: 1 μm streptavidin-coated magnetic particles (Sigma Aldrich, Germany) were functionalized with biotin-modified DNA strands (MWG Eurofins, Germany) (Table S1) by mixing a high excess of DNA (10 μM) with the 1 μm (3 pM) particles in a 0.5x TBE buffer. After incubation for 30 min at room temperature, biotin-DNA-modified particles were purified from the excess of biotin-DNA by centrifugating the sample for 5 min at 15,871 rcf followed by three additional washing steps at same rotation speed. In each step, the supernatant liquid was carefully removed, while keeping the pallet of the magnetic nanoparticles at the bottom of the centrifugation tube by a strong permanent magnet.

biotin-ACCAGATACACCACTCTTCC	biotin-ACTTCTATCAATGCACCTCC
biotin-ACGCATTGCACCGCACGACC	biotin-TCCCAAGTCACCTAATCGCC

coupling of magnetic particles to tile-tubes

Table S1: Staple sequences used for coupling DNA tile-tubes to magnetic particles. Biotin-modified sequences of oligonucleotides that were used to couple magnetic particles to tile-tube structures via the hybridization of complementary DNA strands. Sequences are written from 5´ to 3´.

Coupling of DNA tile-tube structures to magnetic beads. For the construction of DNA tile-tube magnetic bead hybrids from Figure 1g-i, 1μl of biotin-DNA 1μm particles (~32 pM) were hybridized to 3μl of 8HTs, 8HT+s (~26 ng/μl) and 13HTs ((~42 ng/μl), respectively, in a total volume of 100μl 0.5x TBE buffer with 11 mM $MgCl_2$ and 0.05% Tween 20. The conjugation step took place at room temperature for 30 min. To avoid sedimentation of the assembled structures, the samples were put on a rotator at moderate speed.

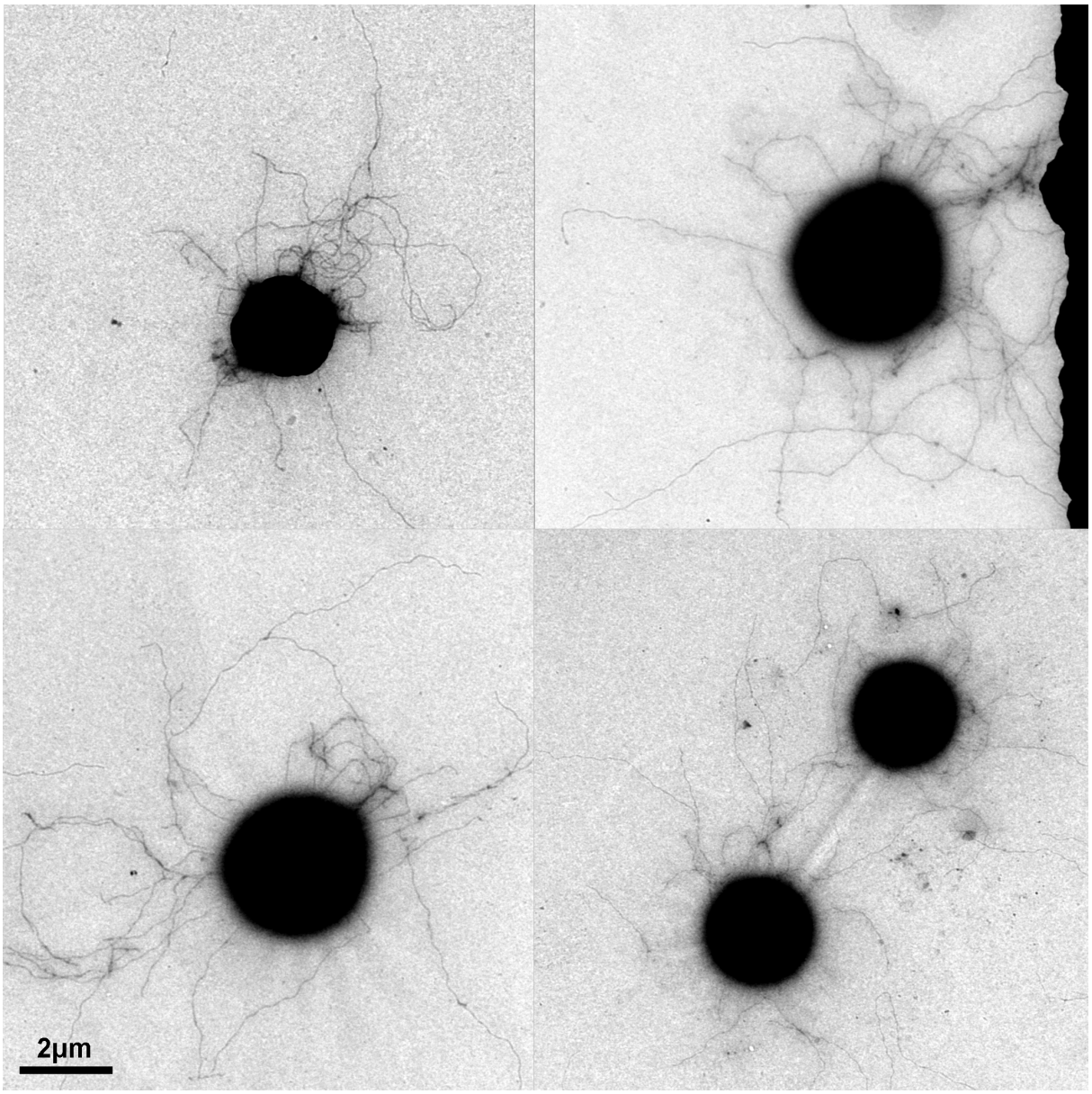

Figure S5: Structural characterization of DNA tile-tube magnetic bead hybrids. Transmission electron microscopy images of purified tw8HTs attached to 1μm magnetic beads. Scale bars: 1 μm

Supplementary Note S2: Fluorescence microscopy and magnetic actuation

To visualize tile tubes via fluorescence microscopy, three out of n tiles of an n-helix tube were modified with Cy3 dyes on their 5´ ends as described in Schiffels et *al* [2] We used a Zeiss Observer Z1 in fluorescence mode with a 100x objective, mercury lamp illumination, a Cy3 filter set and an Andor Solis camera (pixel resolution: 6.4 pixels/μm). All experiments were carried out at room temperature.

DNA - magnetic bead hybrids were actuated by a water-cooled three-axis Helmholtz coil that was incorporated into the microscopy setup. The coil generates a spatially homogeneous time-varying magnetic field, which exerts a torque on the magnetic bead. The magnetic actuation was initiated before the sample was placed into the setup to allow for an instantaneous bundle formation of the hybrid particles in the absence of a close-by surface. However, observation of the hybrid structures was not possible until the structures sank into the focus volume close to the glass surface. Initiation of the magnetic actuation after the particles reached the focus, however, did not lead to bundle formation due to the close proximity with the (sticky) glass surface (we therefore could not observe the dynamics of bundle formation). Similarly, switching the magnetic field off while the swimmers were near the surface led to swimmers attaching to the surface, even though the glass surface was previously functionalized with BSA.
After actuation 10% of the tw8HT and st8HT and 1% of the stw13HT hybrid structures formed a bundle on one side of the bead. Next to these well-assembled bundles, a variety of unwanted side products formed (*e.g.* bundles protruding from two sides of a magnetic particle, clusters of magnetic beads, appendages with (multiple) bifurcations, particles adhering to the surface) as demonstrated for the tw8HT in Figure S6. Hybrids that formed a corkscrew-like bundled tail on one side of the bead started to propel along the rotation axis, whereas particles with bundles on two sides did not. Figure S7 shows the speed distribution of tw8HT swimmers driven by an externally applied magnetic field with frequencies of 1, 2 and 3 Hz.
We further compared the bundle structure of tw8HTs and st8HTs after bundle formation. As demonstrated in Figure S7, both swimmer types show very similar bundle structures resulting in swimmers of similar speeds. The difference in the model parameters - gained from fluorescence intensity measurements - between a tw8HT and a st8HT can be smaller than that between two tw8HT swimmers (see Table S2), which is why we cannot determine a qualitative difference in the bundle structure of the two swimmer types.
The speed of stw13HT hybrid structures varied between 0 and 0.56 μm/s, which is similar to the speed of tw8HT swimmers. However, our fluorescence data indicates that well-assembled corkscrew-like stw13HT bundles consist of fewer tubes (see Figure S9). We speculate that the combination of higher stiffness of the stw13HT (~2.64 times [2]) and fewer tubes in the bundle result in a comparable overall bundle stiffness of tw8HT and stw13HT swimmers, which in turn leads to similar swimming speeds.
Because stw13HT did form with a far lower yield and because we did not observe a difference between tw8HT and st8HT bundles, we focused our study on the tw8HT swimmers, which provided us with a sufficiently broad variety of bundles of different stiffness for testing our theoretical model.

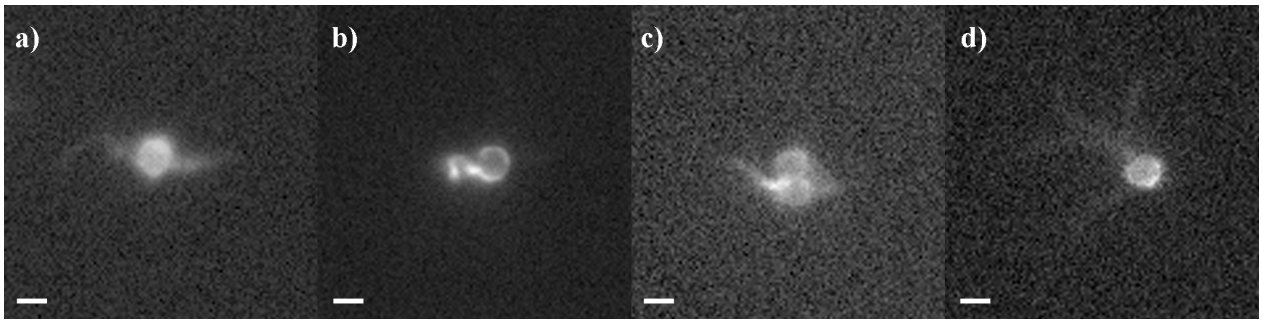

Figure S6: Unwanted tw8HT shapes that formed during bundle formation. Besides properly formed flagellar bundles shown in Figure 2 of the main text, hybrid structures can a) form bundles on two sides of a particle, b) have deformed bundles, c) cluster due to magnetic interaction between to or more particles or d) attach to the glass surface before bundle formation can occur. All scale bars: 2 μm.

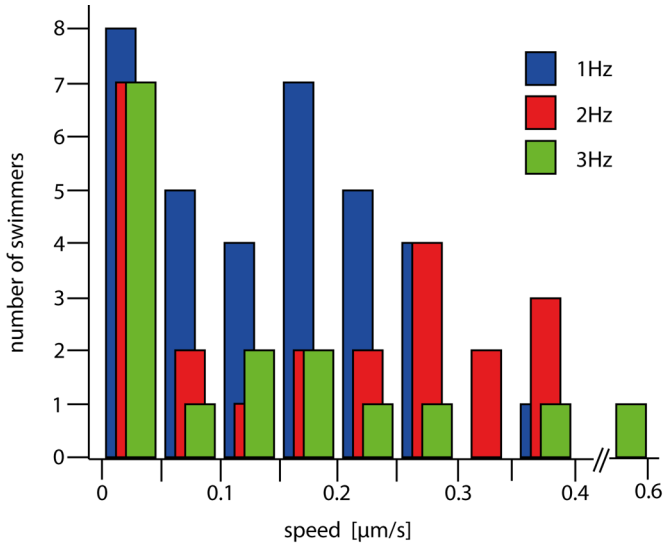

Figure S7: Speed of tw8HT DNA-magnetic bead hybrid swimmers. Histogram shows the speed distribution of artificial swimmers driven by an externally applied magnetic field with frequencies of 1 Hz (blue), 2 Hz (red) and 3 Hz (green), respectively.

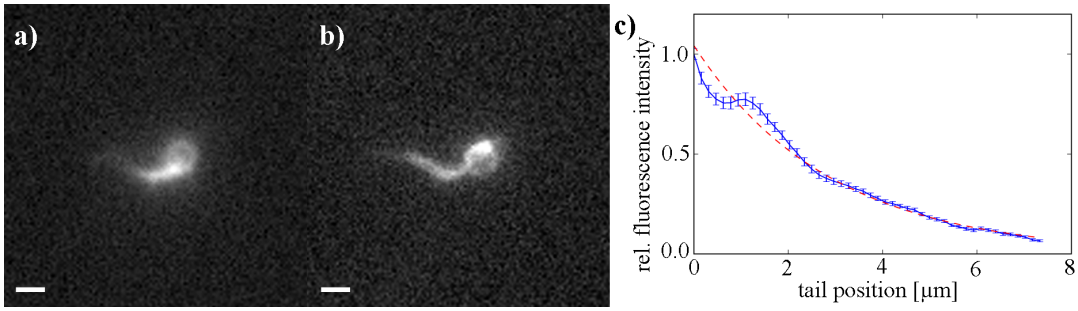

Figure S8: Comparison of the tw8HT and st8HT bundle structure. Snapshots of a) a st8HT swimmer and of b) the tw8HT swimmer #9 from Figure 4. Both swimmers have comparable speeds (0.28 and 0.31 μm/s, respectively) and form similar helical shapes. c) A fluorescence intensity analysis of the bundle from a) shows that the amount of tubes decreases exponentially as in tw8HT bundles. All model parameters and the predicted swimming speed (shown in the inset) agree well with those found for tw8HT swimmers in Table S2. All scale bars: 2 μm.

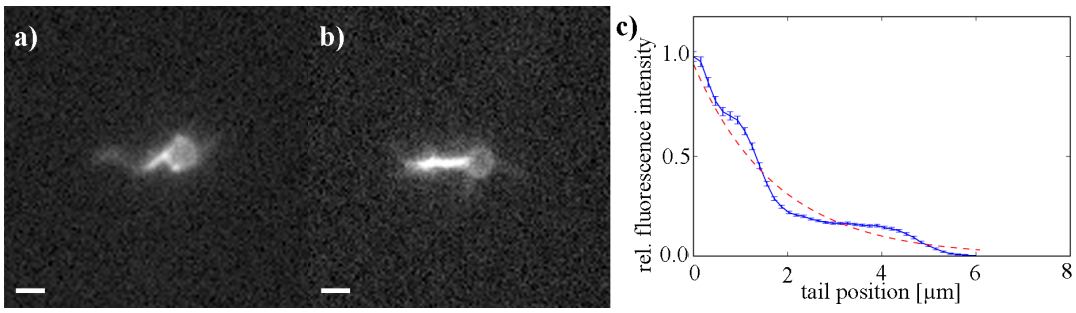

Figure S9: Bundle formation of stw13HT. Among the stw13HT hybrids with a single bundle on one side of the bead, we observed a heterogeneous population of a) proper corkscrew-like and b) arbitrarily shaped structures. c) An analysis of the fluorescence intensity along the bundle of the stw13HT swimmer from a) indicates that its bundle consists of only approximately five tubes. All scale bars: 2μm.

Supplementary Note S3:

Model for swimmers with length-dependent bending modulus

Solving the equations of motion in a hydrodynamic setting is notoriously difficult, rendering adroit simplifications inevitable for an analytic treatment. As a first step, we neglect hydrodynamic fluctuations so that the model becomes deterministic. Without noise, we lose any notion of diffusion, but since we are mainly interested in active swimming here, this is acceptable. The swimmer basically consists of a spherical head with several thin appendages. The main text showed that the attached tubes become entangled through the driven rotation and thus form a tight bundle. Consequently, we the following calculations treat the whole bundle as a *single* thin appendage. This filament is flexible and accordingly has many degrees of freedom, so the main task is to determine its shape. The structure of this supplement is roughly as follows: First, we present a general treatment of flexible filaments with variable stiffness in a small-slope approximation. The shape equation of this filament is then solved with the boundary condition for a spherical bead at one end. From this filament shape, we then determine the swimming speed. Finally, we apply this model to the experimentally realized swimmers from the main text.

Equations of motion for the tail

Actuated swimmers have been discussed in-depth by Lauga,[5] however only for tails with constant stiffness. In the following, we generalize this work to tails with variable stiffness. Because the following line of argument closely resembles the steps in Lauga's work, we try to be brief and focus on the differences. As argued in the main text, we model the bundle of attached tubes as a *single* inextensible elastic filament with a bending stiffness $\alpha(s)$ that changes along the contour of the filament. The elastic energy of the filament with length-dependent bending modulus is given by

$$\mathcal{E} = \int_0^L \Big(\big(\alpha(s)\partial_s^2 \mathbf{r}\big)^2 + \big(\sigma(s)\partial_s \mathbf{r}\big)^2 \Big)\, \mathrm{d}s \ , \tag{1}$$

where $\sigma(s)$ is a Lagrange multiplier ensuring inextensibility of the filament. We stress that both $\alpha(s)$ and $\sigma(s)$ depend on the position s along the filament. From the energy Eq. 1 the force density due to bending and constraint forces are obtained via variation of the contour path. In the low-Reynolds number regime where inertia plays no role, this force needs to balance with the anisotropic friction forces on the filament from the fluid as given by standard slender body theory,[6,7]

$$\big(\xi_\parallel \mathbf{t}\otimes\mathbf{t} + \xi_\perp(1-\mathbf{t}\otimes\mathbf{t})\big)\mathbf{u} = -\partial_s^2\big(\alpha(s)\partial_s^2\mathbf{r}\big) + \partial_s\big(\sigma(s)\partial_s\mathbf{r}\big) \ . \tag{2}$$

Here $\mathbf{t}(s) = \partial_s \mathbf{r}(s)$ is the local tangent to the filament and $\mathbf{u}(s) = \dot{\mathbf{r}}(s)$ is the local speed of the filament with respect to the surrounding fluid. Note the difference on the RHS to the original work of Lauga, where the term $\partial_s^2\big(\alpha(s)\partial_s^2\mathbf{r}\big)$ is replaced by $\alpha\,\partial_s^4\mathbf{r}$. An equation for the Lagrange multiplier which ensures the constraint $|\mathbf{t}^2| = 1$ is given in an implicit form by

$$\mathbf{t}\cdot\partial_s\mathbf{u} = 0 \ . \tag{3}$$

These two equations have the boundary conditions

$$\mathbf{F}_{\text{ext}} = \quad \partial_s(\alpha\,\partial_s^2\mathbf{r}) - \sigma\partial_s\mathbf{r}, \qquad \mathbf{T}_{\text{ext}} = -\mathbf{t}\times\alpha\,\partial_s^2\mathbf{r} \quad \text{at } s=0, \tag{4a}$$

$$\mathbf{F}_{\text{ext}} = -\partial_s(\alpha\,\partial_s^2\mathbf{r}) + \sigma\partial_s\mathbf{r}, \qquad \mathbf{T}_{\text{ext}} = +\mathbf{t}\times\alpha\,\partial_s^2\mathbf{r} \quad \text{at } s=L, \tag{4b}$$

where $\mathbf{F}_{\text{ext}}$ and $\mathbf{T}_{\text{ext}}$ are externally applied forces and torques on the filament, respectively. We remark, that a drag force from the bead is also called "external" in this nomenclature.

Small-slope approximation

The compound head-tail object is torqued into a steady rotation by the externally applied rotating homogeneous magnetic field. The rotation of the head creates a rotating fluid flow around the head that falls off with $1/r$. This is true for both externally and internally actuated swimmers, though the head of externally actuated swimmers co-rotates with the tail whereas for internally actuated swimmers it counter-rotates. In both cases however, this rotational fluid flow is small over the major part of the bundle, so it will be neglected in what follows.

After the swimmer has reached a stationary shape, the magnetic field rotates the head about the axis in which it propels himself and the attachment point of the bundle follows a circular path on the bead surface. We choose this rotation axis as the $\hat{\mathbf{e}}_x$ direction and the orthogonal vectors $\hat{\mathbf{e}}_y$ and $\hat{\mathbf{e}}_z$ as the local coordinate system that co-rotates with the head (Fig. S1). As long as the rotations about the y and z axes are small, it is straight-forward to find this coordinate system. The origin of this coordinate system is placed at the projection of the attachment point on the rotation axis of the swimmer. Consequently, the origin does not coincide with the center of the head, but is offset by some distance in the range $[0,\, r_b]$ where r_b is the bead radius.

The actuation of the bundle is about the x-axis in this coordinate system. In the following

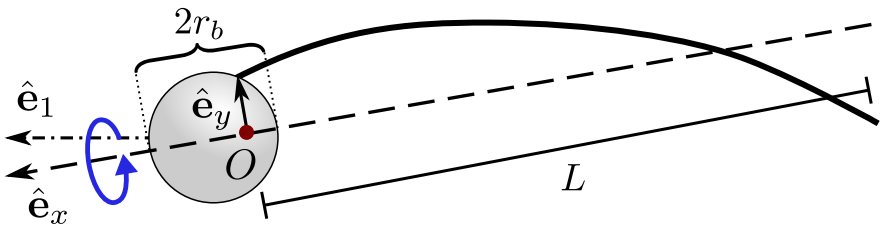

Scheme S1: Coordinate system of the swimmer. The local coordinate system of the swimmer is indicated by $\hat{\mathbf{e}}_x$ and $\hat{\mathbf{e}}_y$. The origin of this coordinate system is at the projection of the attachment point on the x-axis, indicated by O (red dot). The swimmer rotates around the $\hat{\mathbf{e}}_x$ axis (blue arrow). The effective swimming direction $\hat{\mathbf{e}}_1$ is slightly off the $\hat{\mathbf{e}}_x$ axis, because the $\hat{\mathbf{e}}_x$ axis precesses with a small opening angle around the $\hat{\mathbf{e}}_1$ axis. The arrows indicate the direction of the coordinate directions.

we assume small actuations of the bundle about the x-axis, such that $s \approx x$ and

$$\mathbf{r} \approx x\,\hat{\mathbf{e}}_x + y(x,t)\,\hat{\mathbf{e}}_y + z(x,t)\,\hat{\mathbf{e}}_z \ , \tag{5}$$

where $y(s,t)$ and $z(s,t)$ are the small amplitudes along the contour. Equations Eq. 2 and Eq. 3 written in this coordinate frame become with the definitions $\gamma = \xi_\perp/\xi_\parallel$ and $\mathbf{r}_\perp(x,t) = y(x,t)\,\hat{\mathbf{e}}_y + z(x,t)\hat{\mathbf{e}}_z$,

$$\xi_\parallel u_x + (\xi_\parallel - \xi_\perp)(u_y y' + u_z z') = \sigma' \tag{6a}$$

$$u_y\left(\xi_\perp - (\xi_\parallel - \xi_\perp)z'^2\right) + (\xi_\parallel - \xi_\perp)(u_x + u_z z')\,y' = -\partial_x^2(\alpha\,y'') + \partial_x(\sigma\,y') \tag{6b}$$

$$u_z\left(\xi_\perp + (\xi_\parallel - \xi_\perp)z'^2\right) + (\xi_\parallel - \xi_\perp)(u_x + u_y y')\,z' = -\partial_x^2(\alpha\,z'') + \partial_x(\sigma\,z') \tag{6c}$$

$$\alpha\cdot\Big((\frac{1}{\gamma}-1)\mathbf{r}_\perp''\mathbf{r}_\perp^{(4)} - \mathbf{r}_\perp'\mathbf{r}_\perp^{(5)}\Big) - (\frac{2}{3\gamma}+\frac{7}{3})\mathbf{r}_\perp'\mathbf{r}_\perp^{(4)}\alpha' - (\frac{1}{\gamma}+2)\mathbf{r}_\perp'\mathbf{r}_\perp^{(3)}\alpha'' + \frac{1}{\gamma}\mathbf{r}_\perp'\mathbf{r}_\perp^{(3)}\sigma + \sigma'' = 0\ . \tag{6d}$$

Here and in the following a prime denotes a derivative with respect to x. Note the appearance of terms with α' and α'' in the equation for σ.

This set of equations is greatly simplified by an order of magnitude analysis. If $\mathbf{r}_\perp$ is of order ε, σ must be of order ε^2 by Eq. 6d. Likewise by (6a-6c) u_x is of order ε^2 and $u_\perp$ of

order ε. Keeping only terms of leading order, Eq. 6 simplify to

$$\xi_\parallel u_x + (\xi_\parallel - \xi_\perp)(u_y y' + u_z z') = \sigma' \tag{7a}$$

$$\xi_\perp u_y + \partial_x^2(\alpha\, y'') = 0 \tag{7b}$$

$$\xi_\perp u_z + \partial_x^2(\alpha\, z'') = 0\ . \tag{7c}$$

The corresponding small-amplitude approximation of the boundary conditions Eq. 4 for a bundle of length L are

$$\mathbf{F}_{\text{ext}} = \quad \partial_x(\alpha\, \partial_x^2 \mathbf{r}_\perp) - \sigma \hat{\mathbf{e}}_x, \qquad T_{\text{ext},y} = -\alpha\, \partial_x^2 z \qquad T_{\text{ext},z} = \quad \alpha\, \partial_x^2 y \quad \text{at } s = 0 \tag{8a}$$

$$\mathbf{F}_{\text{ext}} = -\partial_x(\alpha\, \partial_x^2 \mathbf{r}_\perp) + \sigma \hat{\mathbf{e}}_x, \qquad T_{\text{ext},y} = \quad \alpha\, \partial_x^2 z \qquad T_{\text{ext},z} = -\alpha\, \partial_x^2 y \quad \text{at } s = L. \tag{8b}$$

Natural units

It is convenient to use intrinsic units such that all pre-factors are numbers. The externally applied magnetic field revolves in the yz-plane with an angular speed ω and periodically actuates the swimmer, hence time is best measured in multiples of ω^{-1}. Only a single tube can extend towards the far end of the bundle, therefore $\alpha(L)$ must be the stiffness of a single tube. It is a natural unit to stiffness in units of the stiffness of a single tube, so that $A(x) \equiv \alpha(x)/\alpha(L)$ becomes the number of tubes making up the bundle at position x. For elasto-hydrodynamic equations the intrinsic bending length $\ell_\omega = \big(\alpha(L)/\omega\xi_\perp\big)^{1/4}$ is a natural unit for the length.[8] Forces and torques are measured by $\xi_\perp \ell_\omega$ and $\xi_\perp \ell_\omega^3$, respectively. In the following we will only refer to the dimensionless quantities but use the same symbols as before.

Free swimmer with head

In the preceding sections we developed the equations of motion of the tail in the small amplitude approximation. The next step is to employ this equation of motion when the tail

is attached to a freely movable bead. The motion of the bead shall be given by the velocity $\mathbf{U}(t)$ and rotation speed $\mathbf{\Omega}(t)$. Given the current speed of the bead, the total speed with respect to the fluid $\mathbf{u}$ of any point on the bundle is then a superposition of the velocity and rotation of the bead coordinate system and the local bundle velocity in the reference frame of the bead:

$$u_x = U_x + z\Omega_y - y\Omega_z \qquad u_y = U_y + x\Omega_z - z\Omega_x + \dot{y} \qquad u_z = U_z + y\Omega_x - x\Omega_y + \dot{z} \tag{9}$$

Because the local coordinate system co-rotates with the head, the tail shape becomes static in these coordinates and $\dot{y} = \dot{z} = 0$. In the low-Reynolds number regime drag through motion and rotation must balance with external force and torque,

$$\tilde{\mathbf{F}}_{\text{ext}} = -\begin{pmatrix} \mathcal{R}_{\parallel}^{FU} & 0 & 0 \\ 0 & \mathcal{R}_{\perp}^{FU} & 0 \\ 0 & 0 & \mathcal{R}_{\perp}^{FU} \end{pmatrix} \tilde{\mathbf{U}} \qquad \tilde{\mathbf{T}}_{\text{ext}} = -\begin{pmatrix} \mathcal{R}_{\parallel}^{L\Omega} & 0 & 0 \\ 0 & \mathcal{R}_{\perp}^{L\Omega} & 0 \\ 0 & 0 & \mathcal{R}_{\perp}^{L\Omega} \end{pmatrix} \tilde{\mathbf{\Omega}} \,,$$

when taken with respect to the center of mass of the bead. When expressed in the shifted local coordinate system these equations become

$$\mathbf{F}_{\text{ext}} = -\begin{pmatrix} \mathcal{R}_{\parallel}^{FU} & 0 & 0 \\ 0 & \mathcal{R}_{\perp}^{FU} & 0 \\ 0 & 0 & \mathcal{R}_{\perp}^{FU} \end{pmatrix} \cdot \mathbf{U} + \begin{pmatrix} 0 & 0 & 0 \\ 0 & 0 & a\mathcal{R}_{\perp}^{FU} \\ 0 & -a\mathcal{R}_{\perp}^{FU} & 0 \end{pmatrix} \cdot \mathbf{\Omega} \tag{10a}$$

$$\mathbf{T}_{\text{ext}} = \begin{pmatrix} 0 & 0 & 0 \\ 0 & 0 & -a\mathcal{R}_{\perp}^{FU} \\ 0 & a\mathcal{R}_{\perp}^{FU} & 0 \end{pmatrix} \cdot \mathbf{U} - \begin{pmatrix} \mathcal{R}_{\parallel}^{L\Omega} & 0 & 0 \\ 0 & \mathcal{R}_{\perp}^{L\Omega} + a^2\mathcal{R}_{\perp}^{FU} & 0 \\ 0 & 0 & \mathcal{R}_{\perp}^{L\Omega} + a^2\mathcal{R}_{\perp}^{FU} \end{pmatrix} \cdot \mathbf{\Omega} \,, \tag{10b}$$

where a is the offset of the origin from the center of the head (see Fig. S1). Because the external magnetic field is strong enough to ensure a phase-locked rotation of the head, we take $\Omega_x = -1$ as given. However, for the remaining components, the forces need to balance

out. Therefore with Eq. 8 we find for the attached end of the tail

$$\mathcal{R}_{\parallel}^{FU} U_x = \quad \sigma(0) \tag{11a}$$

$$\mathcal{R}_{\perp}^{FU} U_y - a\mathcal{R}_{\perp}^{FU} \Omega_z = -\partial_x (A(x) y''(x,t))|_{x=0} \tag{11b}$$

$$\mathcal{R}_{\perp}^{FU} U_z + a\mathcal{R}_{\perp}^{FU} \Omega_y = -\partial_x (A(x) z''(x,t))|_{x=0} \tag{11c}$$

$$a\mathcal{R}_{\perp}^{FU} U_z + (\mathcal{R}_{\perp}^{L\Omega} + a^2 \mathcal{R}_{\perp}^{FU}) \Omega_y = -A(0) z''(0) \tag{11d}$$

$$-a\mathcal{R}_{\perp}^{FU} U_y + (\mathcal{R}_{\perp}^{L\Omega} + a^2 \mathcal{R}_{\perp}^{FU}) \Omega_z = \quad A(0) y''(0) \tag{11e}$$

and for the free end at $x = L$ where no external force applies

$$y''(L) = z''(L) = y^{(3)}(L) = z^{(3)}(L) = \sigma(L) = 0 \ . \tag{12}$$

With the driving of the bundle

$$y(0) = \Re[\varepsilon_1] \qquad\qquad y'(0) = \Re[\varepsilon_2] \tag{13a}$$

$$z(0) = \Im[\varepsilon_1] \qquad\qquad z'(0) = \Im[\varepsilon_2] \tag{13b}$$

there are eight boundary conditions (13, 12) for the two fourth order equations for y and z and two boundary conditions 11a, 12 for the second order equation for σ. For each of the unknowns y, z, σ, U_x, U_y, U_z, Ω_y, Ω_z there is a determining function 6, 11b-11e. As long as the rotation about the y and z axes remains small, we can safely assume that the swimmer revolves mainly about the x-axis with an angular speed ω. We will argue below that this condition is well met in our experiment.

Rewriting Eq. 7b, 7c in natural units and using Eq. 9 yields

$$U_y + x\Omega_z + z + \partial_x^2 (A\, y'') = 0 \tag{14a}$$

$$U_z - x\Omega_y - y + \partial_x^2 (A\, z'') = 0 \tag{14b}$$

where we have used $\Omega_x = -1$. With the definitions $\zeta = y + \imath z$, $U = U_y + \imath U_z$ and $\Omega = \Omega_y + \imath \Omega_z$ these two equations can be combined into one complex equation

$$U + \imath x\Omega - \imath\zeta + \partial_x^2(A\,\zeta'') = 0 \tag{15}$$

with boundary conditions corresponding to (12, 13)

$$\zeta(0) = \varepsilon_1 \qquad \zeta'(0) = \varepsilon_2 \qquad \zeta''(L) = 0 \qquad \zeta^{(3)}(L) = 0\ . \tag{16}$$

Inversion of the equation system 11b and 11e determines U and Ω in terms of x and y:

$$U_y = -\frac{\mathcal{R}_\perp^{L\Omega} + a^2\mathcal{R}_\perp^{FU}}{\mathcal{R}_\perp^{L\Omega}\mathcal{R}_\perp^{FU}}\,\partial_x\big(A(x)\,y''(x,t)\big)\big|_{x=0} + \frac{aA(0)}{\mathcal{R}_\perp^{L\Omega}}y''(0) \tag{17a}$$

$$U_z = -\frac{\mathcal{R}_\perp^{L\Omega} + a^2\mathcal{R}_\perp^{FU}}{\mathcal{R}_\perp^{L\Omega}\mathcal{R}_\perp^{FU}}\,\partial_x\big(A(x)\,z''(x,t)\big)\big|_{x=0} + \frac{aA(0)}{\mathcal{R}_\perp^{L\Omega}}z''(0) \tag{17b}$$

$$\Omega_y = \frac{a}{\mathcal{R}_\perp^{L\Omega}}\,\partial_x\big(A(x)\,z''(x,t)\big)\big|_{x=0} - \frac{A(0)}{\mathcal{R}_\perp^{L\Omega}}z''(0) \tag{17c}$$

$$\Omega_z = \frac{-a}{\mathcal{R}_\perp^{L\Omega}}\,\partial_x\big(A(x)\,y''(x,t)\big)\big|_{x=0} + \frac{A(0)}{\mathcal{R}_\perp^{L\Omega}}y''(0) \tag{17d}$$

With the abbreviations

$$\beta = A(0)\frac{\mathcal{R}_\perp^{L\Omega} + a^2\mathcal{R}_\perp^{FU}}{\mathcal{R}_\perp^{L\Omega}\mathcal{R}_\perp^{FU}} \qquad \sigma = A(0)\frac{a}{\mathcal{R}_\perp^{L\Omega}}$$

$$\lambda = -A(0)\frac{a}{\mathcal{R}_\perp^{L\Omega}} + A'(0)\frac{\mathcal{R}_\perp^{L\Omega} + a^2\mathcal{R}_\perp^{FU}}{\mathcal{R}_\perp^{L\Omega}\mathcal{R}_\perp^{FU}} \qquad \mu = -A(0)\frac{1}{\mathcal{R}_\perp^{L\Omega}} + A'(0)\frac{a}{\mathcal{R}_\perp^{L\Omega}}$$

these relations can be written in a more compact form

$$U = -\big(\beta\zeta^{(3)}(0) + \lambda\zeta''(0)\big) \qquad \Omega = -\imath\big(\sigma\zeta^{(3)}(0) + \mu\zeta''(0)\big)\ . \tag{18}$$

Using this result in Eq. 15 yields the final form

$$-\imath\zeta + \partial_x^2(A\,\zeta'') = (\beta + \sigma x)\zeta^{(3)}(0) + (\lambda + \mu x)\zeta''(0)\ . \tag{19}$$

The major challenge is to find a solution ζ for variable $A(x)$. Lauga has presented an analytic solution for constant A. For a variable $A(x)$ however, we could only find numerical solutions to this equation.

Determining the swimming speed

From the bundle shape the swimming speed will be determined in the following. For this Eqs. 7b, 7c are substituted into Eq. 7a which reads in natural units

$$u_x - (1-\gamma)\big(y'\partial_x^2(A\,y'') + z'\partial_x^2(A\,z'')\big) = \gamma\sigma'\ . \tag{20}$$

Here $\gamma = \xi_\perp/\xi_\parallel$ is the ratio of the drag coefficient perpendicular and parallel to the bundle. Using Eq. 11a and Eq. 9, integration along the contour of the bundle yields

$$\begin{aligned}(\gamma\mathcal{R}_\parallel^{FU} + L)U_x = \Omega_z\int_0^L y\,\mathrm{d}x - \Omega_y\int_0^L z\,\mathrm{d}x + (1-\gamma)\\ \left(A(0)|\mathbf{r}_\perp''(0)|^2 - \mathbf{r}_\perp'(0)\cdot\Big(A(0)\mathbf{r}_\perp^{(3)}(0) + A'(0)\mathbf{r}_\perp''(0)\Big) + \int_0^L A(x)\,\mathbf{r}_\perp''(x)\cdot\mathbf{r}_\perp^{(3)}(x)\mathrm{d}x\right)\ .\end{aligned} \tag{21}$$

Note that with our choice of coordinates, this relation is time-independent. It is straightforward to express this equation in terms of the complex quantities

$$\begin{aligned}(\gamma\mathcal{R}_\parallel^{FU} + L)U_x = \Im\left[\Omega^*\int_0^L \zeta\,\mathrm{d}x]\right] + (1-\gamma)\\ \Re\left[A(0)|\zeta''(0)|^2 - \zeta'(0)^*\Big(A(0)\zeta^{(3)}(0) + A'(0)\zeta''(0)\Big) + \int_0^L A(x)\,\zeta''(x)\zeta^{(3)}(x)^*\mathrm{d}x\right]\ .\end{aligned} \tag{22}$$

Integration along the bundle of Eq. 15 with the boundary conditions (11b, 11c) yields the relation

$$\int_0^L \zeta \,\mathrm{d}x = \imath\big(\mathcal{R}_\perp^{FU} + L\big)U + \Big(a\mathcal{R}_\perp^{FU} - \frac{L^2}{2}\Big)\Omega \;, \tag{23}$$

therefore $\Im[\Omega^* \int_0^L \zeta \,\mathrm{d}x] = (\mathcal{R}_\perp^{FU} + L)\,\Re[\Omega^* U]$. With the expressions for Ω and U from Eq. 18 one finds

$$\Re[\Omega^* U] = \frac{A(0)^2}{\mathcal{R}_\perp^{FU}\mathcal{R}_\perp^{L\Omega}} \Im[\zeta''(0)\zeta^{(3)}(0)^*] \;. \tag{24}$$

Collecting the previous results, the final expression for the swimming speed in the local frame of reference becomes

$$\begin{aligned}(\gamma\mathcal{R}_\parallel^{FU} + L)U_x =& A(0)^2 \frac{\mathcal{R}_\perp^{FU} + L}{\mathcal{R}_\perp^{FU}\mathcal{R}_\perp^{L\Omega}} \,\Im[\zeta''(0)\zeta^{(3)}(0)^*] + \\ & (1-\gamma)\,\Re\Big[A(0)|\zeta''(0)|^2 - \zeta'(0)^*\Big(A(0)\zeta^{(3)}(0) + A'(0)\zeta''(0)\Big) + \int_0^L A(x)\,\zeta''(x)\zeta^{(3)}(x)^* \mathrm{d}x\Big] \;.\end{aligned} \tag{25}$$

Transformation into the lab system

The swimming speed in Eq. 25 refers to a local coordinate system that co-rotates with the swimmer's head. Therefore, it must be transformed into the laboratory system. We define the lab frame along the orthogonal vectors $\hat{\mathbf{e}}_1$, $\hat{\mathbf{e}}_2$, $\hat{\mathbf{e}}_3$, where $\hat{\mathbf{e}}_1$ points along the average swimming direction. The swimmer revolves at constant angular velocity $\{\Omega_x = -1,\, \Omega_y,\, \Omega_z\}$ about its local axes. Hence, in the lab system the local coordinate vectors change according to

$$\frac{\mathrm{d}}{\mathrm{d}t}\mathbf{e}_{xyz} = \begin{pmatrix} 0 & -\Omega_z & \Omega_y \\ \Omega_z & 0 & -1 \\ -\Omega_y & 1 & 0 \end{pmatrix} \cdot \mathbf{e}_{xyz} \;. \tag{26}$$

The analytical solution of this rotation is given through the matrix exponential $\Re[\exp(M\,t)] \cdot \mathbf{e}_{xyz}$ where M is the above rotation matrix. Dropping all terms of second order in Ω one

finds

$$\hat{\mathbf{e}}_x = \hat{\mathbf{e}}_1 - \Re[\Omega(1-\mathrm{e}^{\imath t})]\,\hat{\mathbf{e}}_2 - \Im[\Omega(1-\mathrm{e}^{\imath t})]\,\hat{\mathbf{e}}_3 \tag{27a}$$

$$\hat{\mathbf{e}}_y = -\Re[\Omega(1-\mathrm{e}^{-\imath t})]\,\hat{\mathbf{e}}_1 + \cos t\,\hat{\mathbf{e}}_2 + \sin t\,\hat{\mathbf{e}}_3 \tag{27b}$$

$$\hat{\mathbf{e}}_x = -\Im[\Omega(1-\mathrm{e}^{-\imath t})]\,\hat{\mathbf{e}}_1 - \sin t\,\hat{\mathbf{e}}_2 + \cos t\,\hat{\mathbf{e}}_3 \tag{27c}$$

which is exact up to order $|\Omega|^2$. The total swimming velocity of the head is given by $\mathbf{U} = U_x\hat{\mathbf{e}}_x + U_y\hat{\mathbf{e}}_y + U_z\hat{\mathbf{e}}_z$ of which we are only interested in the $\hat{\mathbf{e}}_1$ component. Hence,

$$U_1 = U_x - \Re[\Omega(1-\mathrm{e}^{-\imath t})]U_y - \Im[\Omega(1-\mathrm{e}^{-\imath t})]U_z\ . \tag{28}$$

In contrast to the velocity in co-rotating coordinates, this expression depends on time due to the oscillating motion of the bead. However, the time-dependent terms average out over one period, such that

$$\langle U_1\rangle = U_x - \Re[\Omega^* U]\ . \tag{29}$$

With the previous results from (24,25) this yields the swimming speed in the lab system

$$\langle U_1\rangle = \frac{1}{\gamma\mathcal{R}_\parallel^{FU} + L}\Bigg(A(0)^2\frac{\mathcal{R}_\perp^{FU} - \gamma\mathcal{R}_\parallel^{FU}}{\mathcal{R}_\perp^{FU}\mathcal{R}_\perp^{L\Omega}}\,\Im[\zeta''(0)\zeta^{(3)}(0)^*] + (1-\gamma)\,\Re\Big[A(0)|\zeta''(0)|^2 - \zeta'(0)^*\Big(A(0)\zeta^{(3)}(0) + A'(0)\zeta''(0)\Big) + \int_0^L A(x)\,\zeta''(x)\zeta^{(3)}(x)^*\mathrm{d}x\Big]\Bigg)\ . \tag{30}$$

Because the experimentally implemented swimmer has a spherical head for which $\mathcal{R}_\perp^{FU} = \mathcal{R}_\parallel^{FU}$ and $\mathcal{R}_\perp^{L\Omega} = \mathcal{R}_\parallel^{L\Omega}$, this expression simplifies further to

$$\langle U_1\rangle = \frac{1-\gamma}{\gamma\mathcal{R}^{FU} + L}\Bigg(\frac{A(0)^2}{\mathcal{R}^{L\Omega}}\Im[\zeta''(0)\zeta^{(3)}(0)^*] + \Re\Big[A(0)|\zeta''(0)|^2 - \zeta'(0)^*\Big(A(0)\zeta^{(3)}(0) + A'(0)\zeta''(0)\Big) + \int_0^L A(x)\,\zeta''(x)\zeta^{(3)}(x)^*\mathrm{d}x\Big]\Bigg)\ . \tag{31}$$

For $A = const$ this result is consistent with the one from the work of Lauga. The conversion of this result into physical coordinates is accomplished by multiplying the result with $\ell_\omega \cdot 2\pi f$ where f is the rotation frequency of the external magnetic field. The extra factor of 2π is necessary because the natural unit of time is given by *angular* frequency ω^{-1} and not frequency f^{-1}.

The applicability of this result depends on the solvability of Eq. 19. When fixed to a solid wall where the RHS of Eq. 19 becomes zero, an analytic solution for ζ can be found. For a free swimmer however, the inhomogeneous equation has to be solved which we could only achieve numerically. We did this with Mathematica where in a first step the equation was solved numerically with $\zeta''(0)$ and $\zeta^{(3)}(0)$ on the RHS as parameters. In a second step we matched these intermediate parameters to the actual derivative of the numerical solution through a root-finding algorithm. The integrated residual of the so-obtained solution was of the order 10^{-6} per unit length and therefore negligibly small.

Stiffness model and parameter estimation

Our model depends on several parameters which we group in global and individual ones. The global parameters are well controlled and need no discussion. These are the fluid viscosity ($\eta \approx 1\,mPa\,s$ at $20°C$), the persistence length of one fibre ($8.2\,\mu m$,[2]), the frequency at which the magnetic field was rotated ($f = 1$–$3\,Hz$) and the head diameter ($1\,\mu m$). We note that the head appears visually enlarged on the video material by its high brightness, but this is misleading. Electron-microscopy of the same batch of beads revealed that their diameter was well within specification.

The individual parameters varied for different swimmers, so they had to be determined for each swimmer instance. These are the bundle length, the number of tubes in the bundle, the amplitude parameters ε_1 and ε_2 and their respective phase. The bundle length could be determined from snapshots of the swimmer by integrating the contour length of the bundle. Typical values of the bundle length range from 4.8–8.0 μm (Tab. S2), which is consistent

with TEM measurements.

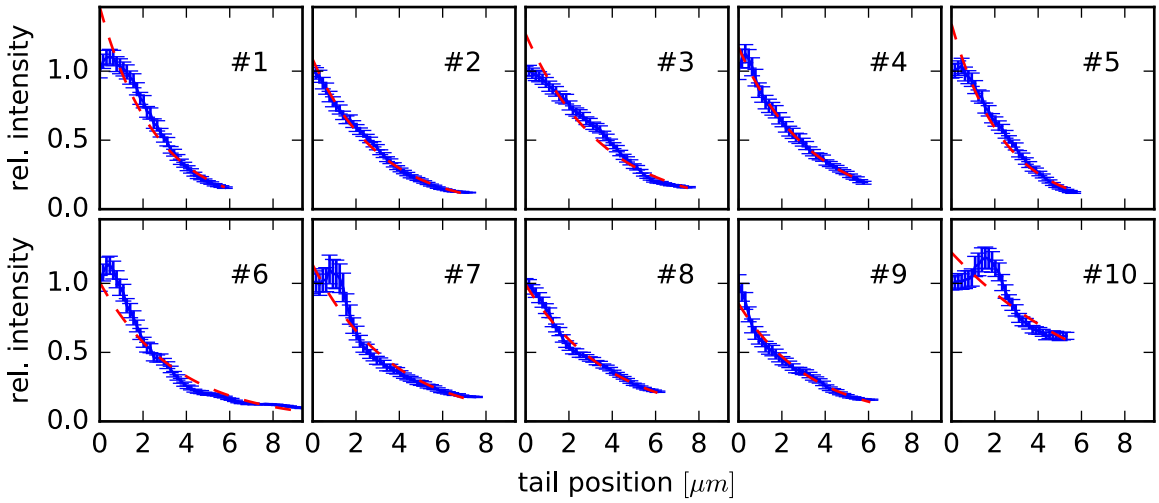

Figure S10: Fluorescence intensity of DNA tile-tube bundles. The data show the fluorescence intensity profiles of the bundles of ten different swimmers from Figure 4 (blue, with standard error). Data was gained by averaging over several movie frames to rule out possible errors due to a change in the fluorescence distribution along the particle during a rotation. These data were fit with an exponential (dashed red) in order to determine the decay length χ of the attached tails (for numerical values see Table S2).

Beside length, a stiffness model $A(x)$ has to be chosen. Because each tube of the tail results from a linear polymerization process, we expect an exponential distribution of tube lengths.[9] Yin[1] found an exponential length distribution in the length of unbound DNA tubes. To verify this length distribution, we measured the fluorescence intensity along the contour of the bundle which we expect to be proportional to the number of tubes. Figure 3a shows the expected exponential drop in fluorescence intensity, therefore we assumed that the number of tubes in the bundle scales as $N_0 \mathrm{e}^{-s/\chi}$. Without cross-links the stiffness scales linearly with the number of tubes in the tail,[10–12] therefore we take $A(x) = N_0 \mathrm{e}^{-x/\chi}$ as the stiffness model. The parameters N_0 and χ could be estimated by an exponential fit of the fluorescence intensity, if we assume that one single tube extends to the far end (see Fig. fig:decay-lengths). Typical numbers of attached tubes N_0 range from 7 to 25, which is consistent with TEM pictures of the hybrids. We note, that the increased swimming speed is a generic feature of decreasing tail stiffness and is also found for other stiffness decay

functions. In particular, our model also applies if the stiffness scales differently with the number of filaments, e.g. $\alpha(x) \propto n^a$, because this only amounts to a change of the decay length $\alpha(x) \propto \mathrm{e}^{x/(\chi/a)}$. Additional cross-links among the filaments increase a,[10–12] so that the effects from a thinning bundle become even stronger.

The amplitude parameters ε_1 and ε_2 have a major impact on the swimming speed. This can be seen in the formula for the swimming speed Eq. 30, where ζ enters quadratically in each term. Because the tail amplitude ζ depends as a rule of thumb linearly on both ε_1 and ε_2, the swimming speed reacts quadratically on their values. Consequently, these parameters must be determined carefully, which is challenging due to the small size of the swimmers. For that, we took snapshots of the video sequence where the tail was maximally deflected. This allowed to measure the amplitude of the attachment point, ε_1, in fractions of the bead radius and we found values ranging from 0.1–1.0. Likewise, the opening angle θ between tail and swimming direction was measured for which we found values ranging from 20–40 degrees. This opening angle θ determines ε_2 via $\varepsilon_2 = \tan\theta$. The relative phase of ε_1 and ε_2 corresponds to the torsion of the tail close to the head. Without loss of generality we take ε_2 as real. From our data it was not possible to reliably determine the phase difference, therefore it had to be estimated. Because the tail is pulled through the fluid, it feels a drag directed against its current direction of movement and bends accordingly. This induced bending corresponds to a phase shift of $-\pi/2$ which we take as an estimate for the phase shift. We note that the phase shift has only a minor impact on the swimming speed of about 5%.

Finally the friction coefficients of tail and bead need to be estimated. For the tail, the friction coefficient can be calculated via slender-body theory,[6,7] where we assumed an aspect ratio of 200 for the tail bundle resulting in $\gamma \approx 1.6$. The Stokes friction coefficients of a solid sphere are given by

$$\mathcal{R}_\perp^{FU} = \mathcal{R}_\parallel^{FU} = 6\pi\eta\, r_b \qquad\qquad \mathcal{R}_\perp^{L\Omega} = \mathcal{R}_\parallel^{L\Omega} = 8\pi\eta\, r_b^3 \,, \tag{32}$$

where η is the fluid viscosity and r_b the head radius. In the experiment, translational motion is free, so that $\mathcal{R}^{FU}$ is a reasonable value for the translational friction. On the other hand, the bead rotation is *not* free, because the external magnetic field aligns the magnetic moment of the bead with its direction. As a consequence, a torque on the bead works against the magnetic field and therefore has a much smaller effect. To emulate this suppressed rotation, we scaled the rotational friction coefficient by a large factor (500). Because the resulting values of the swimming speed differ by only 20% in the range $[200, \infty]$, the error inflicted by this arbitrariness is small.

Table S2: Model parameters and swimming speeds for the swimmers from Figure 4

swimmer	#1	#2	#3	#4	#5	#6	#7	#8	#9	#10
length $[\mu m]$	6.2	7.8	6.8	6.5	6.3	8.0	6.5	6.0	4.8	7.0
χ $[\mu m]$	2.60	3.08	3.54	3.28	2.43	3.55	3.67	3.88	3.36	7.27
frequency $[Hz]$	1	1	1	2	1	1	1	2	2	1
$\varepsilon_1/\mathrm{e}^{-\imath\pi/2}$ $[r_b]$	0.9	1.	0.9	0.25	0.5	0.1	0.9	0.5	0.9	0.8
$\arctan(\varepsilon_2)$ $[deg]$	21	20	20	26	26	30	28	23	30	42
measured speed $[\mu m/s]$	0.12	0.12	0.17	0.19	0.20	0.22	0.25	0.27	0.31	0.42
predicted speed $[\mu m/s]$	0.16	0.14	0.12	0.18	0.20	0.15	0.19	0.16	0.36	0.29

Table S2 shows the model parameters and predicted swimming speeds for ten swimmers from the experiment corresponding to Figure 4. Typically, we measured swimming speeds around $0.2\,\mu m/s$, and our predicted swimming speeds were off by less than 40%. This agreement is completely satisfactory, considering that some parameters could only be estimated and that this calculation was done in the approximation of small amplitudes.

A great advantage of the theoretical model is that different stiffness profiles can be easily compared. In particular, the swimming speed of constant stiffness versus variable stiffness can be compared as shown in Figure 3c. It is remarkable, that the swimming speed for variable stiffness outperforms a bundle of equal length tubes for all parameters shown. This behaviour is valid over the entire parameter range we looked at and is no coincidence of a particular parameter choice but a general feature of thinning bundles of passive flagella.

References

(1) Yin, P.; Hariadi, R. F.; Sahu, S.; Choi, H. M.; Park, S. H.; Labean, T. H.; Reif, J. H. *Science* **2008**, *321*, 824–826.

(2) Schiffels, D.; Liedl, T.; Fygenson, D. K. *ACS Nano* **2013**, *7*, 6700–6710.

(3) Dietz, H.; Douglas, S. M.; Shih, W. M. *Science* **2009**, *325*, 725–730.

(4) Castro, C. E.; Kilchherr, F.; Kim, D. N.; Shiao, E. L.; Wauer, T.; Wortmann, P.; Bathe, M.; Dietz, H. *Nat. Methods* **2011**, *8*, 221–229.

(5) Lauga, E. *Phys. Rev. E* **2007**, *75*, 041916.

(6) Keller, J. B.; Rubinow, S. I. *Journal of Fluid Mechanics* **1976**, *75*, 705–714.

(7) Batchelor, G. K. *Journal of Fluid Mechanics* **1970**, *44*, 419–440.

(8) Wiggins, C. H.; Riveline, D.; Ott, A.; Goldstein, R. E. *Biophys. J.* **1998**, *74*, 1043–1060.

(9) Flory, P. J. *J. Am. Chem. Soc.* **1936**, *58*, 1877–1885.

(10) Claessens, M. M. A. E.; Bathe, M.; Frey, E.; Bausch, A. R. *Nature Materials* **2006**, *5*, 748–753.

(11) Heussinger, C.; Bathe, M.; Frey, E. *Physical Review Letters* **2007**, *99*, 048101.

(12) Bathe, M.; Heussinger, C.; Claessens, M. M. A. E.; Bausch, A. R.; Frey, E. *Biophys. J.* **2008**, *94*, 2955–2964.

This material is available free of charge via the Internet at `http://pubs.acs.org/`.